

## The induced electric field distribution in the solar atmosphere \*

Rong Chen<sup>1,2</sup>, Zhi-Liang Yang<sup>1,2</sup> and Yuan-Yong Deng<sup>2</sup>

<sup>1</sup> Department of Astronomy, Beijing Normal University, Beijing 100875, China;  
[zlyang@bnu.edu.cn](mailto:zlyang@bnu.edu.cn)

<sup>2</sup> Key Laboratory of Solar Activity, National Astronomical Observatories, Chinese Academy of Sciences, Beijing 100012, China

Received 2012 November 7; accepted 2013 February 28

**Abstract** A method of calculating the induced electric field is presented. The induced electric field in the solar atmosphere is derived by the time variation of the magnetic field when the accumulation of charged particles is neglected. In order to derive the spatial distribution of the magnetic field, several extrapolation methods are introduced. With observational data from the Helioseismic and Magnetic Imager aboard NASA's *Solar Dynamics Observatory* taken on 2010 May 20, we extrapolate the magnetic field from the photosphere to the upper atmosphere. By calculating the time variation of the magnetic field, we can get the induced electric field. The derived induced electric field can reach a value of  $10^2$  V cm<sup>-1</sup> and the average electric field has a maximum point at the layer 360 km above the photosphere. The Monte Carlo method is used to compute the triple integration of the induced electric field.

**Key words:** Sun: magnetic fields — Sun: atmosphere — Sun: activity

### 1 INTRODUCTION

The electric field in the solar atmosphere plays an important role in heating plasma, and accelerating and transporting charged particles (Priest & Forbes 2000). At the same time, its distribution provides rich information about solar flares, as well as other dynamic solar activities. The simultaneous determination of electric and magnetic field vectors enable an estimation of Poynting flux of electromagnetic energy entering the corona and the flux of relative magnetic helicity. However, the determination of the electric field is quite harder, with values smaller than the magnetic field in the solar atmosphere.

Although the solar activities are dominated by the magnetic field, and much progress has been made in this aspect in the past decades, there are still many points beyond our understanding, such as the physical mechanisms of flares and filament eruptions. It is time to determine whether the electric field, its magnitude, geometry, time-dependence and especially spatial distribution, can provide us with powerful tools to probe solar activities where particle acceleration and energy release are believed to occur.

Wien (1916) is the first author who proposed measuring the electric field of solar plasma and measured the motional electric field using the Stark effect. Around 1980, some attempts to measure

---

\* Supported by the National Natural Science Foundation of China.

the electric field with helium and silicon spectra had been made, which suggested an electric field of  $700 \text{ V cm}^{-1}$  (Davis 1977) and  $300 \text{ V cm}^{-1}$  (Jordan et al. 1980) respectively. Even so, Moran & Foukal (1991) pointed out that direct measurement of the electric field by the Stark effect is hard to perform with low sensitivity.

Because there was not an efficient and reliable way to directly measure the electric field of the solar atmosphere, researchers investigated many indirect methods, which either explicitly or implicitly assume ideal magnetohydrodynamics (MHD),  $\mathbf{E} = -\mathbf{v} \times \mathbf{B}/c$ . The tracking method and inductive method are two classes of such techniques.

According to the ideal MHD equation above, the magnetic field is known from the vector magnetogram, so both of the classes have focused on determining the velocity vector. The tracking method, developed by November & Simon (1988), computes velocity through a cross-correlation function that depends on the shift of feature points between two images. Although tracking methods are simple and robust, they also suffer from some shortcomings, for example, this technique is actually two-dimensional without a vertical component. Inductive methods, first developed by Kusano et al. (2002), improve the result of tracking methods with a solution to the vertical component from the magnetic induction equation and derive a three-component velocity vector from a sequence of vector magnetograms. Since the seminal work of Kusano et al. (2002), several techniques have been developed to determine velocity from vector magnetograms, and Welsch et al. (2007) provided detailed tests and comparisons of these techniques.

Poletto & Kopp (1986) derived the maximum electric field of  $2 \text{ V cm}^{-1}$  in a large two-ribbon flare using the reconnection theory of Priest & Forbes (2000) where they used a very simple relationship between the electric field along the current sheet and the observable velocity and magnetic field. With a similar theory, Wang et al. (2003) discovered two stages of electric evolution in another two-ribbon flare: as a first stage, the electric field remains at the value  $1 \text{ V cm}^{-1}$ , which represents an average over 20 minutes, and is followed by a value of  $0.1 \text{ V cm}^{-1}$  over the next 2 hours. Qiu et al. (2002) worked on an impulsive flare with high cadence  $\text{H}\alpha$  observations at Big Bear Solar Observatory (BBSO) and estimated the maximum electric field to be  $90 \text{ V cm}^{-1}$ .

Recently, Fisher et al. (2010) proposed a way to compute the electric field from a sequence of vector magnetograms by using Faraday's law and showed that it is possible to derive an electric field whose curl is the time derivative of three components of  $\mathbf{B}$ . The main problem for these authors is the non-unique solution of Faraday's law.

In this paper, our goal is to present a method to indirectly compute the three-components of the induced electric field distribution in the solar atmosphere through evolution of a vector magnetic field. We first extrapolate the magnetic field from the photosphere to the corona, and then calculate the induced electric field from the time variation of the magnetic field.

In solar plasma, there are three kinds of electric fields: a static electric field, induced electric field and motional electric field. Here we only focus on the induced electric field, which is caused by a change in the magnetic field. The static electric field, which is triggered by an accumulation of charged particles, and the motion of plasma in the direction perpendicular to the magnetic field are not considered due to the screening of plasma in the solar atmosphere.

The paper is structured as follows. In Section 2 we extrapolate the vector magnetic field distribution from a magnetogram; in Section 3 we compute the electric field from the extrapolated magnetic field; and in Section 4 we give an evaluation by use of the observational vector magnetograms from Helioseismic and Magnetic Imager aboard NASA's *Solar Dynamics Observatory* (HMI/SDO). The conclusion and discussion are given in Section 5.

## 2 EXTRAPOLATION OF MAGNETIC FIELD

At present, although many attempts have been made to estimate the coronal magnetic field (House 1977; Arnaud & Newkirk 1987; Judge 1998; Judge et al. 2001), reliable information about the mag-

netic field is only available for the photosphere. Similar to the electric field, we currently, and in the near future, have to face the fact that direct measurements of the magnetic field in the global solar atmosphere are still unavailable.

There are many methods to extrapolate the magnetic field from the photospheric magnetic field under the assumption that the magnetic field is nearly force-free. A force-free magnetic field of the solar atmosphere must satisfy the following equations:

$$\mathbf{j} \times \mathbf{B} = 0, \quad (1)$$

$$\nabla \times \mathbf{B} = \alpha \mathbf{B}, \quad (2)$$

$$\nabla \cdot \mathbf{B} = 0, \quad (3)$$

where  $\alpha$  is a scalar function of position and time. The above equations imply the Lorentz force is absent and  $\alpha$  is a constant along the magnetic field line. The equations represent a potential field if  $\alpha = 0$ , a current-carrying linear force-free (LFF) field if  $\alpha = \text{constant}$ , and a general nonlinear force-free (NLFF) field if  $\alpha = f(\mathbf{r})$ .

The extrapolations of potential and LFF fields are maturely developed. The potential and LFF fields can be determined directly from the line-of-sight (LOS) component of the magnetic field (e.g. MDI/SOHO) as an input, and  $\alpha$  has to be computed in an LFF field from some additional data (Chiu & Hilton 1977; Seehafer 1978; Alissandrakis 1981; Gary 1989).

For the NLFF field, several methods have already been proposed: the Grad-Rubin method (Sakurai 1981), the MHD relaxation method (Chodura & Schlueter 1981; Roumeliotis 1996) and the optimization method (Wheatland et al. 2000). The last one will be used in this paper.

In the optimization approach, Wheatland et al. (2000) defined a quantity  $L$

$$L = \int_V [B^{-2} |(\nabla \times \mathbf{B}) \times \mathbf{B}|^2 + |\nabla \cdot \mathbf{B}|^2] dV, \quad (4)$$

where  $\mathbf{B}$  is defined in a volume  $V$ . If  $L$  is decreased to zero and Equations (1)–(3) are fulfilled, then the field is force-free in the volume  $V$ . In order to reduce  $L$ ,  $\mathbf{B}$  needs to evolve like

$$\frac{\partial \mathbf{B}}{\partial t} = \mu \mathbf{F}. \quad (5)$$

Wheatland et al. (2000) tested the optimization method. Inhester & Wiegmann (2006) provided a detailed comparison of the optimization and Grad-Rubin methods by implementing these two algorithms and comparing their performance. In addition, Liu et al. (2011b) used two semi-analytical solutions of force-free fields to test two other NLFF extrapolation methods: the boundary integral equation (BIE) method developed by Yan & Sakurai (2000) and the approximate vertical integration (AVI) method developed by Song et al. (2006).

Wiegmann (2004) improved the optimization approach by showing how the magnetic field can be reconstructed only from the bottom boundary and developed a code which will be used later.

Moreover, although the NLFF field model is widely-used (Régnier & Amari 2004; Wiegmann et al. 2005; Schrijver et al. 2008), a joint study by De Rosa et al. (2009) concluded that a successful application of NLFF field extrapolation should satisfy several requirements. Recently Wiegmann et al. (2012) offered a detailed discussion of this problem and proved that their results fulfill these requirements. The results of NLFF modeling should be used with some caution.

### 3 CALCULATING INDUCED ELECTRIC FIELD DISTRIBUTION

In the solar atmosphere, the static electric field is neglected due to plasma screening. We consider the case where there is no accumulation of charged particles in the solar atmosphere, and the electric field is mainly generated from the time variation of the magnetic field. That is,

$$\nabla \cdot \mathbf{E} = 0, \quad (6)$$

and

$$\nabla \times \mathbf{E} = \mathbf{\Omega}, \quad (7)$$

where

$$\mathbf{\Omega} = -\frac{\partial \mathbf{B}}{\partial t}. \quad (8)$$

We could derive the electric field directly from the time variation of the magnetic field (Batchelor 2000)

$$\mathbf{E} = \frac{1}{4\pi} \iiint_D \frac{\mathbf{\Omega}(\xi, \eta, \zeta) \times \mathbf{R}}{R^3} d\xi d\eta d\zeta. \quad (9)$$

In order to derive  $\mathbf{E}$  from Equation (9), we introduce the Monte Carlo method which is a numerical simulation method to solve the triple integral problem. This method can be used to approximate the integral if a precise value of the integral is not important and estimating its value is enough, or if it is not possible to calculate a precise value.

If  $f(x, y, z)$  is a continuous function on domain  $D$ , and  $g(x, y, z)$  is a probability density function such that

$$\iiint_D g(x, y, z) dx dy dz = 1, \quad (10)$$

$(x_i, y_i, z_i) (i = 1, 2, \dots, N)$  are a sequence of random numbers that fall in domain  $D$ , and according to the basic theorem of the Monte Carlo method, when  $N$  is large enough, we have

$$\iiint_D f(x, y, z) dx dy dz \approx \frac{1}{N} \sum_{i=1}^N \frac{f(x_i, y_i, z_i)}{g(x_i, y_i, z_i)}. \quad (11)$$

If  $g(x, y, z)$  is constant, Equation (10) becomes

$$g(x, y, z) \iiint_D dx dy dz = \frac{1}{D}, \quad (12)$$

and

$$\iiint_D f(x, y, z) dx dy dz \approx \frac{D}{N} \sum_{i=1}^N f(x_i, y_i, z_i). \quad (13)$$

By applying the Monte Carlo method to Equation (9), we get the final equation of  $\mathbf{E}$  as

$$\mathbf{E} \approx \frac{D}{N \cdot 4\pi} \sum_{i=1}^N \frac{\mathbf{\Omega}(\xi_i, \eta_i, \zeta_i) \times \mathbf{R}}{R^3}. \quad (14)$$

#### 4 THE INDUCED ELECTRIC FIELD IN NOAA AR 11072

To implement the method we described in the previous sections, we provide an example here. First we extrapolate the magnetic field of the photosphere from magnetograms, then we compute the time difference of two magnetic field distributions  $\mathbf{\Omega} = -\partial \mathbf{B} / \partial t$ , and finally we use the Monte Carlo method to calculate the electric field distribution.

In this example, we use observational data from HMI/*SDO* which provides high spatial and temporal resolution vector magnetograms (Schou et al. 2012). HMI provides continuous vector magnetograms at a 12-minute cadence and has released several data series of cutouts of the original full disk images over the past two years. The full released data summary can be found at the *SDO* Joint Science Operations Center webpage (<http://jsoc.stanford.edu>). From the available data releases, we chose the 6-day cutouts of  $512 \times 512$  pixels for NOAA AR 11072 from 2010 May 20 to 2010 May 26.

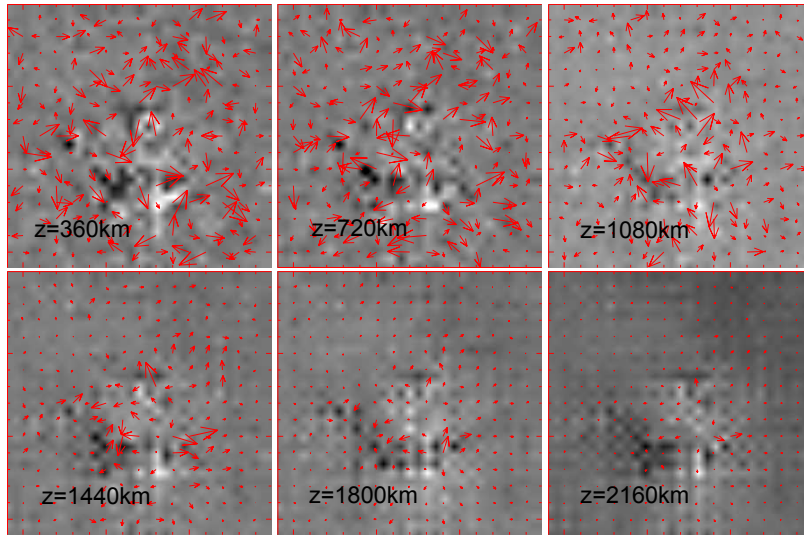


**Fig. 1** Extrapolated results of a magnetogram for AR 11072 observed from HMI/SDO at 12:12 on 2010 May 20. The size of every image is  $10.8 \times 10.8 \text{ Mm}^2$ , and the value of  $z$  means the distance from the photosphere in units of km. Arrows show directions and amplitudes of  $B_x$  and  $B_y$ , while the background image shows the amplitude of  $B_z$ .

We run the code developed by Wiegelmann (2004) (optimization method) to extrapolate the magnetic field from vector magnetograms, and both potential and the NLFF fields are generated. Liu et al. (2011a) provided a detailed comparison of the NLFF and potential fields. We extrapolate the magnetic field to a volume of  $512 \times 512 \times 9$  pixels and the distance between two adjacent pixels is 0.5 arcsec. Figure 1 shows the extrapolated NLFF field of one magnetogram.

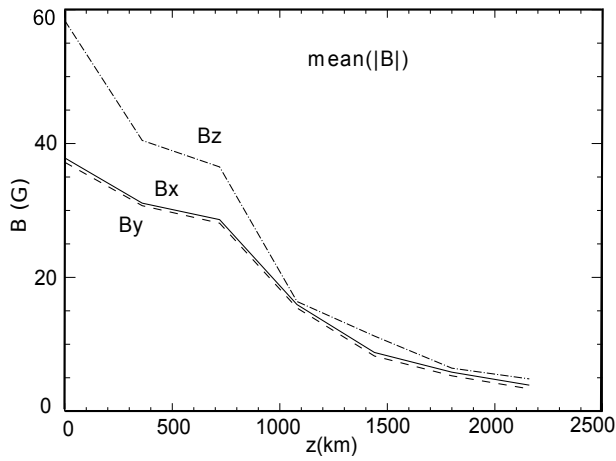
The horizontal cuts of the lower six layers consisting of  $30 \times 30$  pixels are shown in Figure 1. The value of  $z$  indicates height from the photosphere in units of kilometers, arrows show directions and amplitudes of  $B_x$  and  $B_y$ , while the background image shows the amplitude of  $B_z$ .

Table 1 shows the maximum and average value of the three components of the extrapolated magnetic field, and Figure 2 shows the average of the absolute value of the magnetic field at six layers. In Figure 3, we show the difference between two extrapolated results, that is,  $B_2 - B_1$  where  $B_1$  is the magnetic field in Figure 1.

Table 2 shows the maximum and average value for the difference from the extrapolated magnetic field, and Figure 4 shows the average of the absolute value of  $\Delta B$  at six layers. The Monte Carlo method requires that  $\Omega = -\frac{\partial B}{\partial t}$  is a continuous function in Equations (9) and (14), but our observed

**Table 1** Maximum and Average Value of  $B$  at Different Layers

| $Z$<br>(km) | $\max( B_x )$     | $\max( B_y )$     | $\max( B_z )$<br>(G) | $\text{mean}(B_x)$   | $\text{mean}(B_y)$    | $\text{mean}(B_z)$ |
|-------------|-------------------|-------------------|----------------------|----------------------|-----------------------|--------------------|
| 360         | $1 \times 10^3$   | $8.4 \times 10^2$ | $8.3 \times 10^2$    | $4 \times 10^{-1}$   | $-1.1 \times 10^{-1}$ | -3.2               |
| 720         | $1.1 \times 10^3$ | $7.8 \times 10^2$ | $1.1 \times 10^3$    | $7.6 \times 10^{-1}$ | $-1.2 \times 10^{-1}$ | -3.4               |
| 1080        | $7.2 \times 10^2$ | $1.1 \times 10^3$ | $2.7 \times 10^3$    | $6.4 \times 10^{-1}$ | $-9.6 \times 10^{-2}$ | -3.2               |
| 1440        | $8.2 \times 10^2$ | $1 \times 10^3$   | $4.5 \times 10^2$    | $4.5 \times 10^{-1}$ | $-3.3 \times 10^{-2}$ | -3.3               |
| 1800        | $1.9 \times 10^2$ | $4.2 \times 10^2$ | $8.6 \times 10^2$    | $3.9 \times 10^{-1}$ | $-4.4 \times 10^{-2}$ | -3                 |
| 2160        | $2.7 \times 10^2$ | $2.7 \times 10^2$ | $8.1 \times 10$      | $3.2 \times 10^{-1}$ | $-3.3 \times 10^{-2}$ | -3                 |



**Fig. 2** The average of absolute intensity of  $B$  at six layers.

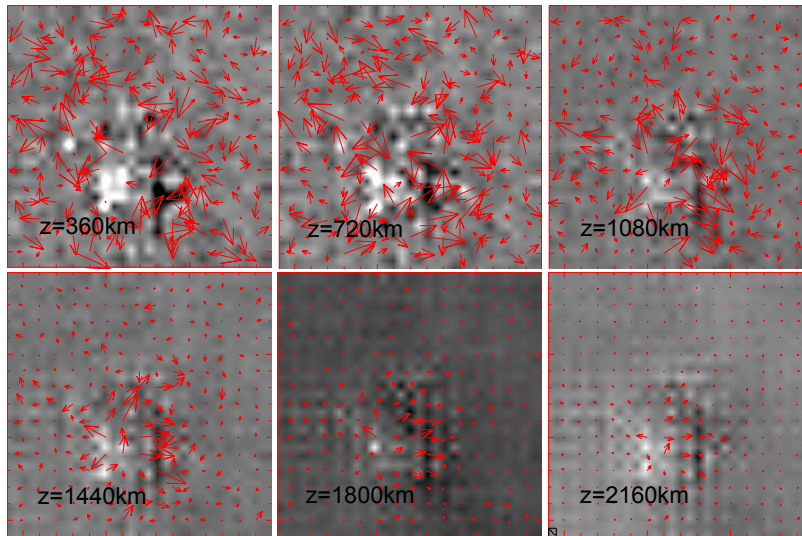


**Fig. 3** Time variation of the magnetic field extrapolated from two continuous vector magnetograms. The first one is observed at 12:12 on 2010 May 20 by HMI/SDO, and the other is observed 12 minutes later.

and extrapolated  $\Omega$  is discrete with a spatial distance of 0.5 arcsec. Thus, we linearize  $\Omega$  in units of 0.5 arcsec to reconstruct a continuous function.

We use the linear algorithm below to compute  $\Omega(x, y, z_{\text{up}})$  of the upper projection in Figure 5:

$$\begin{aligned}\Omega(x, y_{\text{back}}, z_{\text{up}}) &= \Omega(x_{\text{left}}, y_{\text{back}}, z_{\text{up}}) \times (x_{\text{right}} - x)/0.5 + \Omega(x_{\text{right}}, y_{\text{back}}, z_{\text{up}}) \times (x - x_{\text{left}})/0.5, \\ \Omega(x, y_{\text{forth}}, z_{\text{up}}) &= \Omega(x_{\text{left}}, y_{\text{forth}}, z_{\text{up}}) \times (x_{\text{right}} - x)/0.5 + \Omega(x_{\text{right}}, y_{\text{forth}}, z_{\text{up}}) \times (x - x_{\text{left}})/0.5, \\ \Omega(x, y, z_{\text{up}}) &= \Omega(x, y_{\text{back}}, z_{\text{up}}) \times (y_{\text{forth}} - y)/0.5 + \Omega(x, y_{\text{forth}}, z_{\text{up}}) \times (y - y_{\text{back}})/0.5,\end{aligned}$$

**Table 2** Maximum and Average Value of  $\Delta B$  at Different Layers

| $Z$<br>(km) | $\max( \Delta B_x )$ | $\max( \Delta B_y )$ | $\max( \Delta B_z )$<br>(G) | $\text{mean}(\Delta B_x)$ | $\text{mean}(\Delta B_y)$ | $\text{mean}(\Delta B_z)$ |
|-------------|----------------------|----------------------|-----------------------------|---------------------------|---------------------------|---------------------------|
| 360         | $1.2 \times 10^3$    | $1.4 \times 10^3$    | $1.2 \times 10^3$           | $1.5 \times 10^{-1}$      | $1.7 \times 10^{-1}$      | $4.3 \times 10^{-2}$      |
| 720         | $1.1 \times 10^3$    | $1 \times 10^3$      | $1.3 \times 10^3$           | $2.2 \times 10^{-1}$      | $2.7 \times 10^{-3}$      | $4.1 \times 10^{-2}$      |
| 1080        | $7.4 \times 10^2$    | $1.1 \times 10^3$    | $2.7 \times 10^3$           | $-1.7 \times 10^{-1}$     | $1.6 \times 10^{-1}$      | $4.2 \times 10^{-2}$      |
| 1440        | $8.1 \times 10^2$    | $1 \times 10^3$      | $4.8 \times 10^2$           | $-8.9 \times 10^{-2}$     | $-6.4 \times 10^{-3}$     | $3.9 \times 10^{-2}$      |
| 1800        | $1.9 \times 10^2$    | $4.2 \times 10^2$    | $8.7 \times 10^2$           | $-8.8 \times 10^{-2}$     | $6.8 \times 10^{-2}$      | $3.7 \times 10^{-2}$      |
| 2160        | $2.7 \times 10^2$    | $2.6 \times 10^2$    | $8.9 \times 10$             | $-9 \times 10^{-2}$       | $3.7 \times 10^{-2}$      | $3.6 \times 10^{-2}$      |

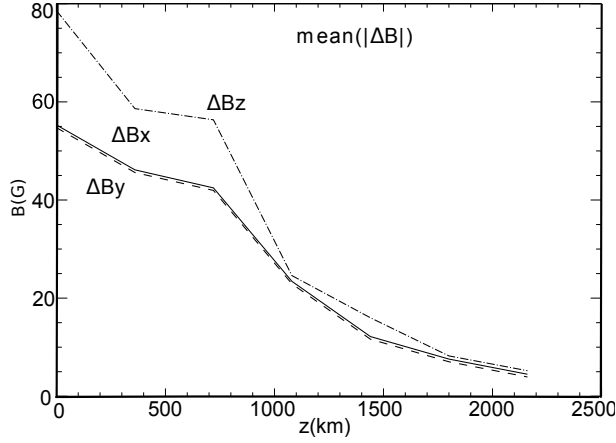


**Fig. 4** The average of absolute intensity of  $\Delta B$  at six layers.

**Table 3** Maximum and Average Value of  $E$  at Different Layers

| $Z$<br>(km) | $\max( E_x )$     | $\max( E_y )$     | $\max( E_z )$<br>(V cm <sup>-1</sup> ) | $\text{mean}(E_x)$    | $\text{mean}(E_y)$    | $\text{mean}(E_z)$    |
|-------------|-------------------|-------------------|--|-----------------------|-----------------------|-----------------------|
| 360         | $5.5 \times 10^2$ | $3.9 \times 10^2$ | $2.5 \times 10^2$                      | $3.5 \times 10^{-3}$  | $1.6 \times 10^{-3}$  | $1.1 \times 10^{-3}$  |
| 720         | $3.6 \times 10^2$ | $1.7 \times 10^2$ | $4.4 \times 10^2$                      | $9 \times 10^{-4}$    | $2.3 \times 10^{-4}$  | $-1.4 \times 10^{-3}$ |
| 1080        | $4.6 \times 10^2$ | $2.3 \times 10^2$ | $1.6 \times 10^2$                      | $2.1 \times 10^{-3}$  | $1.2 \times 10^{-3}$  | $7.9 \times 10^{-4}$  |
| 1440        | $8.1 \times 10$   | $2 \times 10^2$   | $1.1 \times 10^2$                      | $-2.1 \times 10^{-4}$ | $-7.5 \times 10^{-5}$ | $-3.5 \times 10^{-5}$ |
| 1800        | $1.2 \times 10$   | $1.1 \times 10$   | $1.8 \times 10$                        | $-2.7 \times 10^{-4}$ | $-4.3 \times 10^{-4}$ | $-1.6 \times 10^{-4}$ |
| 2160        | $2.2 \times 10$   | $1.2 \times 10$   | 9.3                                    | $-2.2 \times 10^{-5}$ | $-4.1 \times 10^{-4}$ | $-1.2 \times 10^{-4}$ |

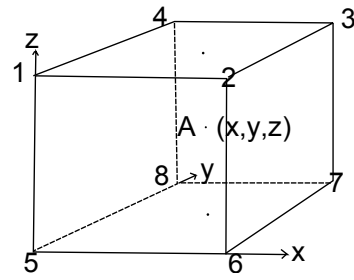
where

$$\begin{aligned}
 x_{\text{left}} &= x_1 = x_4 = x_5 = x_8, x_{\text{right}} = x_2 = x_3 = x_6 = x_7, \\
 y_{\text{back}} &= y_1 = y_2 = y_5 = y_6, y_{\text{forth}} = y_3 = y_4 = y_7 = y_8, \\
 z_{\text{down}} &= z_5 = z_6 = z_7 = z_8, z_{\text{up}} = z_1 = z_2 = z_3 = z_4.
 \end{aligned}$$

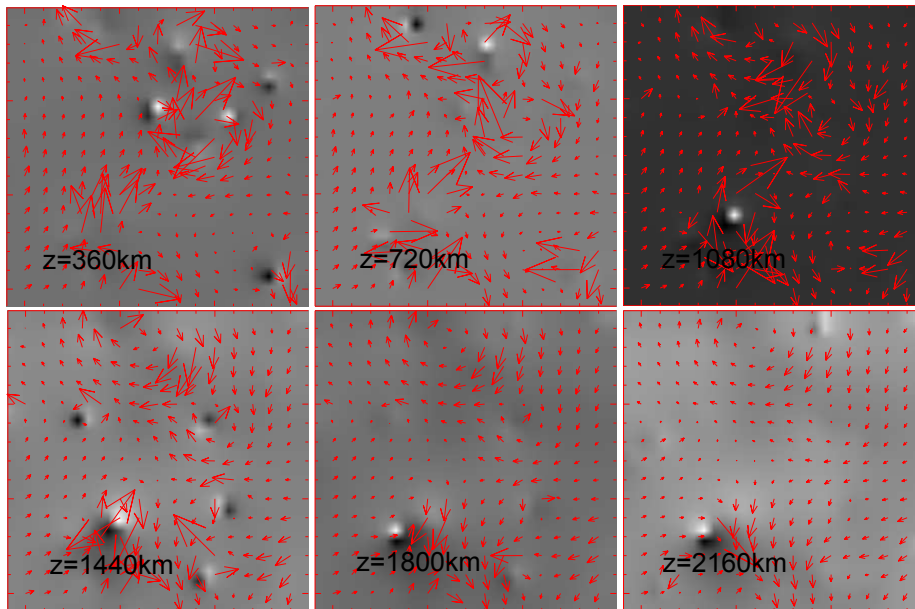
Similarly, we can get  $\Omega(x, y, z_{\text{down}})$ , together with  $\Omega(x, y, z_{\text{up}})$ , and we compute the linearized  $\Omega(x, y, z)$  from

$$\Omega(x, y, z) = \Omega(x, y, z_{\text{down}}) \times (z_{\text{up}} - z)/0.5 + \Omega(x, y, z_{\text{up}}) \times (z - z_{\text{down}})/0.5.$$

To save time, we only generate 10 000 random points in a cube of  $512 \times 512 \times 7$ , and calculate the distribution of the induced electric field following Equation (14). One of our results is shown in Figure 6.



**Fig. 5** The  $\Omega$  at the point  $A(x, y, z)$  is linearized from the eight points adjacent to it. The position of these adjacent points is  $(x_i, y_i, z_i, i = 1 \dots 8)$ , and every edge of the cube represents 0.5 arcsec. Point A has two projections in the upper and lower surfaces where the value of  $\Omega$  should be computed first.



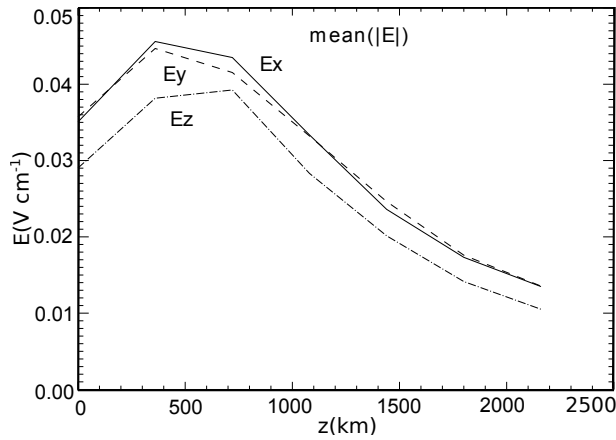
**Fig. 6** Computed “vector electrograms” ( $10.8 \times 10.8 \text{ Mm}^2$ ) of different depths. Arrows show directions and amplitudes of  $E_x$  and  $E_y$ , while the background image shows the amplitude of  $E_z$ .

Table 3 shows the maximum and average value of the three calculated components of the electric field and Figure 7 shows the average of the absolute value of electric field at six layers. The average of the absolute electric field reaches a maximum at the layer 360 km above the photosphere.

## 5 SUMMARY AND DISCUSSION

In this paper, we describe and implement a new method to calculate the distribution of the induced electric field in the solar atmosphere using a sequence of vector magnetograms as an input.

We first introduce several extrapolation methods for the magnetic field and make a simple comparison of these methods, then we choose the optimization method in our example to extrapolate the



**Fig. 7** The average of absolute intensity of  $E$  at six layers.

magnetograms observed by HMI/*SDO* from the photosphere to the corona. We also derive a special solution of the electric field in the form of a triple integral.

To solve the triple integral problem, we utilize the Monte Carlo method to obtain a new equation describing the electric field. As this method requires a continuous function, we linearize  $\Omega$  which is originally a discrete function in the spatial domain. A similar linearization has been used to compute the time variation of the magnetic field from the magnetograms with a 12-minute time resolution, that is, we assume that  $B$  goes through a linear change in this 12-minute interval.

Through the derivation, it is proved that as long as the boundary condition (Batchelor 2000) is fulfilled, we can obtain the three-component electric field of the solar atmosphere from only vector magnetograms. In our example for NOAA AR 11072, the result shows that the intensity distribution of the induced electric field varies at different layers: it reaches a value of  $10^2$  V cm $^{-1}$  and the average electric field has a maximum point at the layer 360 km above the photosphere. However, there are several shortcomings with this method that need to be resolved. First, the boundary condition (Batchelor 2000) is not strictly satisfied, because in the quiet area, time variation of the magnetic field is small but not zero. Secondly, the temporal and spatial resolution of the HMI/*SDO* vector magnetogram is still not high enough to provide continuous time and spatial sequences, so linearization methods have to be used twice in our calculation: one is to compute  $\partial B/\partial t$  which assumes the magnetic field changes linearly over this 720s interval, and the other is to satisfy the requirement of the Monte Carlo method which needs a continuous function in the spatial domain as input. Thus our calculation process might not fully reflect the real situation of the Sun. Finally, we use the Monte Carlo method to compute the triple integration of a large volume, which is a time-consuming job, and we have to adopt a small sample of only 10 000 random numbers, but a larger sample could give more accurate results.

**Acknowledgements** We thank the HMI science team for providing the pre-processed vector magnetograms. We are very grateful to the anonymous referee whose comments and suggestions helped us to improve our manuscript. This work is supported by a grant from the Key Laboratory of Solar Activity at National Astronomical Observatories, Chinese Academy of Sciences. This work is also supported by the National Natural Science Foundation of China (Grant Nos. U1231104, 10921303, 11178005 and 11203036).

## References

- Alissandrakis, C. E. 1981, *A&A*, 100, 197
- Arnaud, J., & Newkirk, G., Jr. 1987, *A&A*, 178, 263
- Batchelor, G. K. 2000, *An Introduction to Fluid Dynamics* (Cambridge University Press), 86
- Chiu, Y. T., & Hilton, H. H. 1977, *ApJ*, 212, 873
- Chodura, R., & Schlueter, A. 1981, *Journal of Computational Physics*, 41, 68
- Davis, W. D. 1977, *Sol. Phys.*, 54, 139
- De Rosa, M. L., Schrijver, C. J., Barnes, G., et al. 2009, *ApJ*, 696, 1780
- Fisher, G. H., Welsch, B. T., Abbett, W. P., & Bercik, D. J. 2010, *ApJ*, 715, 242
- Gary, G. A. 1989, *ApJS*, 69, 323
- House, L. L. 1977, *ApJ*, 214, 632
- Inhester, B., & Wiegmann, T. 2006, *Sol. Phys.*, 235, 201
- Jordan, C., Bartoe, J.-D. F., & Brueckner, G. E. 1980, *ApJ*, 240, 702
- Judge, P. G. 1998, *ApJ*, 500, 1009
- Judge, P. G., Casini, R., Tomczyk, S., Edwards, D. P., & Francis, E. 2001, *NASA STI/Recon Technical Report N*, 2, 27999
- Kusano, K., Maeshiro, T., Yokoyama, T., & Sakurai, T. 2002, *ApJ*, 577, 501
- Liu, S., Zhang, H. Q., & Su, J. T. 2011a, *Sol. Phys.*, 270, 89
- Liu, S., Zhang, H. Q., Su, J. T., & Song, M. T. 2011b, *Sol. Phys.*, 269, 41
- Moran, T., & Foukal, P. 1991, *Sol. Phys.*, 135, 179
- November, L. J., & Simon, G. W. 1988, *ApJ*, 333, 427
- Poletto, G., & Kopp, R. A. 1986, in *The Lower Atmosphere of Solar Flares; Proceedings of the Solar Maximum Mission Symposium, Sunspot*, ed. D. F. Neidig, 453
- Priest, E., & Forbes, T., eds. 2000, *Magnetic Reconnection: MHD Theory and Applications* (Cambridge Univ. Press), 460
- Qiu, J., Lee, J., Gary, D. E., & Wang, H. 2002, *ApJ*, 565, 1335
- Régnier, S., & Amari, T. 2004, *A&A*, 425, 345
- Roumeliotis, G. 1996, *ApJ*, 473, 1095
- Sakurai, T. 1981, *Sol. Phys.*, 69, 343
- Schou, J., Scherrer, P. H., Bush, R. I., et al. 2012, *Sol. Phys.*, 275, 229
- Schrijver, C. J., De Rosa, M. L., Metcalf, T., et al. 2008, *ApJ*, 675, 1637
- Seehafer, N. 1978, *Sol. Phys.*, 58, 215
- Song, M. T., Fang, C., Tang, Y. H., Wu, S. T., & Zhang, Y. A. 2006, *ApJ*, 649, 1084
- Wang, H., Qiu, J., Jing, J., & Zhang, H. 2003, *ApJ*, 593, 564
- Welsch, B. T., Abbett, W. P., De Rosa, M. L., et al. 2007, *ApJ*, 670, 1434
- Wheatland, M. S., Sturrock, P. A., & Roumeliotis, G. 2000, *ApJ*, 540, 1150
- Wiegmann, T. 2004, *Sol. Phys.*, 219, 87
- Wiegmann, T., Inhester, B., Lagg, A., & Solanki, S. K. 2005, *Sol. Phys.*, 228, 67
- Wiegmann, T., Thalmann, J. K., Inhester, B., et al. 2012, *Sol. Phys.*, 281, 37
- Wien, W. 1916, *Annalen der Physik*, 354, 842
- Yan, Y., & Sakurai, T. 2000, *Sol. Phys.*, 195, 89